Materials Advances

ROYAL SOCIETY OF CHEMISTRY

PAPER

Published on 08 July 2026

Cite this: *Mater. Adv.*, 2026, 7, 8439

Role of scandium precursor decomposition in MOCVD of AlScN and predictions for AlYN

Isabel Streicher, †*[a] Arbresha Muriqi, [b] Rita Mullins, [b] Patrik Straňák, [a] Mario Prescher, [a] Manuel Kapitein,[c] Lutz Kirste, [a] Rüdiger Quay, [a] Michael Nolan [b] and Stefano Leone ‡*[a]

Received 21st April 2026,
Accepted 23rd June 2026

DOI: 10.1039/d6ma00563b

rsc.li/materials-advances

Wurtzite $Al_{1-x}Sc_xN$ is a novel nitride that attracts attention for its piezoelectric and ferroelectric properties, and further offers the possibility to grow strain-free AlScN/GaN heterostructures due to an *a* lattice parameter matching with GaN. Growth of AlScN by metal–organic chemical vapor deposition is challenging because of the low vapor pressure of commercially available Sc precursors and a high amount of carbon atoms present in these precursors, that can incorporate into the films. In this work, precursor decomposition and ligand loss of the novel Sc precursors $(EtCp)_2Sc(bdma)$ and $(EtCp)_2Sc(dtbt)$ are studied by density functional theory and related to experimental results. It is found that low temperatures, low pressures, and low NH_3 flows promote carbon incorporation and lead to grey coloration of AlScN films grown with $(EtCp)_2Sc(bdma)$, probably due to the high residual mass of this precursor. At 1100 °C, high quality 2DEGs can be grown, especially with $(EtCp)_2Sc(dtbt)$. Predictions for the growth of AlYN/GaN heterostructures are made.

1. Introduction

Gallium nitride-based wide bandgap semiconductor devices perform in various fields, from optoelectronics to high frequency and high power electronics. Especially radio frequency and power electronics make extensive use of AlGaN/GaN-based high electron mobility transistors (HEMTs).[1,2] The two-dimensional electron gas (2DEG) that forms at the AlGaN/GaN heterointerface can be modulated with a gate contact and thus HEMTs can be used as signal amplifiers or as switches. The sheet charge carrier density (n_s) in the 2DEG determines the channel resistance, the achievable current and power density. AlN barriers can supply very high charge carrier densities but are severely limited by their low critical thickness on GaN and thus relaxation effects that reduce the lifetime of devices.[3] When AlN is alloyed with transition metals such as scandium (Sc) or yttrium (Y), this limitation can be resolved, as both AlScN and AlYN feature an *a* lattice parameter matching with GaN,[4,5] promising for epilayers free of lattice-mismatch induced strain and thus increased device lifetimes. Due to the high intrinsic spontaneous polarization of their barrier layers, these heterostructures still provide very high n_s of 2–5 × 10^{13} cm^{-2} in the case of AlScN and in the range of 1–3 × 10^{13} cm^{-2} for AlYN.[5,6] The possibility to grow strain-free additionally enables the growth of multichannel structures which allows to further increase the achievable drain currents.[7,8] The exact concentration at which the lattice matching occurs, especially in AlScN, is currently a subject of discussion. Early theoretical studies predicted a very narrow window of high accessible thicknesses around 18%,[4] while more recent experimental studies point toward lower values.[9]

Metal–organic chemical vapor deposition (MOCVD) provides high structural quality, high growth rates and is cost-effective in production scale of nitride semiconductors, making it the preferred technique for industrial applications in terms of throughput. First MOCVD-grown AlScN/GaN HEMTs feature an output power (P_{out}) and a power added efficiency (PAE) of 8.4 W mm^{-1} and 42.0% at 30 GHz class-AB continuous wave operation, which is the highest reported combination of P_{out} and a PAE reported at Ka-band frequencies on metal-polar GaN-based HEMTs so far.[10] However, the analysis of reliability measurements revealed that trapping currently limits the device performance of AlScN/GaN HEMTs.[11] Carbon acts as acceptor or donor trap and can reduce the n_s of the 2DEG,[12–14] and leads to high Coulomb scattering and reduced mobilities.[15] It is likely one of the reasons for deterioration in device

[a] *Fraunhofer Institute for Applied Solid State Physics IAF, Tullastrasse 72, 79108 Freiburg, Germany. E-mail: isabel.streicher@cornell.edu, leonestefano@hotmail.com*
[b] *Tyndall National Institute, University College Cork, Lee Maltings, Dyke Parade, Cork T12R5CP, Ireland*
[c] *Dockweiler Chemicals GmbH, Emil-von-Behring-Strasse 76, 35041 Marburg, Germany*
† Present address: Kavli Institute at Cornell for Nanoscale Science, Cornell University, Ithaca, NY, 14853, USA.
‡ Present address: Epitaly Advanced Materials, Via Tuscolana 1717, 00133 Rome, Italy.

performance. The main source for carbon incorporation into MOCVD-grown films are the precursor molecules.[12] This adds a challenge to the Sc precursor selection for the MOCVD of AlScN: the Sc precursors with the lowest carbon over scandium (C/Sc) ratios of 15 and 12, tris-cyclopentadienyl-scandium Cp_3Sc and bis-methylcyclopentadienyl-scandium $(MCp)_2ScCl$, respectively, feature very low vapor pressures. The novel Sc precursors bis-(ethylcyclopentadienyl) (*N*,*N*′-bis(dimethylamino)acetamidinato) scandium $(EtCp)_2Sc$(bdma) and bis(ethylcyclopentadienyl)(di-*tert*-butyl-triazenido) scandium $(EtCp)_2Sc$(dtbt) have increased vapor pressures but C/Sc ratios of 20 and 22, respectively. While carbon incorporation depends not only on the C/Sc ratio of a precursor but also on the decomposition behavior of the precursor molecule and the ligands themselves, it can be assumed that the more carbon is present, the more will incorporate into the film. The ultimate solution for this problem would be the implementation of carbon-free precursors with enhanced vapor pressures as recently shown for GaN and AlN,[16] but currently such precursors are not available for Sc. In the meantime, it is vital to understand the trade-off between enhanced vapor pressure and carbon incorporation.

Growth of Sc-containing nitrides by MOCVD represented a significant challenge because of the very low vapor pressure and thus very low molar flows of the first commercially available Sc precursor Cp_3Sc.[17–20] A modified, heated gas injection system developed for commercial MOCVD systems,[19] and patented by Fraunhofer IAF,[21] allows for molar flows above 1 μmol min^{-1} sufficient for the growth of ternary alloys at bubbler temperatures of up to 155 °C. However, growth rates below 0.015 nm s^{-1} were found to lead to significant thermal budged-induced degradation of the heterointerfaces by interdiffusion of atoms and strain-related effects at process temperatures of 900 °C and higher.[22] This interfacial grading can be drastically reduced by the insertion of a nominal AlN interlayer or by increasing the AlScN growth rate by using the novel Sc precursors with enhanced vapor pressures.[23] These Sc precursors $(EtCp)_2Sc$(bdma) and $(EtCp)_2Sc$(dtbt) are a game changer in AlScN growth as they allow for up to ten times enhanced growth rates and higher control of the Sc incorporation at reduced bubbler temperatures.[23] While promising electrical characteristics of the 2DEGs were demonstrated, the impurity incorporation remains an open question. Depending on the decomposition and stability of the ligands of the novel Sc precursors, the high C/Sc ratios of the precursors favor carbon incorporation into the films. At the same time, carbon incorporation can be reduced by selecting appropriate growth conditions.

This work investigates how the decomposition of $(EtCp)_2Sc$(bdma) and $(EtCp)_2Sc$(dtbt) affects carbon incorporation and the performance of AlScN/GaN heterostructures. To this end, the Sc precursors are simulated with density functional theory (DFT) and bond dissociation energies E^{dissoc} are calculated, while the chemical behavior of the precursors is investigated experimentally by thermogravimetric analysis (TGA). This information is used to interpret the impurity levels of MOCVD-grown 500 nm-thick AlScN films measured by time-of-flight secondary ion mass spectrometry (ToF-SIMS) as well as the 2DEG properties of AlScN/GaN heterostructures grown at temperatures ranging from 900 to 1200 °C determined by Hall effect measurement. Optimum growth conditions for the lowest possible carbon incorporation are identified and implemented to investigate the effect of Sc concentration on the structural quality of the heterostructures by high-resolution X-ray diffraction (HRXRD) and the electrical properties of the 2DEGs by Hall effect measurements.

Further, predictions are made for growth of the novel nitride AlYN with the Y precursor $(EtCp)_2Y$(dtbt), a structural twin to $(EtCp)_2Sc$(dtbt). Growth of AlYN by MOCVD was demonstrated recently and faces challenges analogue to those of AlScN, low vapor pressure of Y precursors and high carbon levels. AlYN/GaN feature 2DEGs with n_s slightly below those of AlScN which allows for higher electron mobilities and lower threshold voltages promising for high-performing HEMT devices.[5,24,25] Unlike Sc, Y is not a critical raw material, it is more abundant and easier to extract and purify and thus promises for higher sustainability.

2. Experimental

2.1. Simulation

We use the Turbomole code for the density functional theory (DFT) simulations of the Sc and Y precursors.[26,27] Turbomole uses localised basis sets for calculations of gas phase species. The PBE0 hybrid exchange–correlation functional which incorporates 25% exact HF exchange, is used with a triple zeta valence polarised basis set (TZVPP) and a medium (m3) integration grid.[28,29] The geometry of all molecules is relaxed with no symmetry using analytic gradients and with a SCF convergence criterion of 10^{-6} Ha in the total energy. The convergence criteria for the geometry was that the maximum norm of the cartesian gradient is less that 10^{-3} Ha.

The energy for ligand elimination (E_{diss}) is computed as follows in eqn (1):

$$E_{diss} = E(Sc(L)_2) + E(L) - E(Sc(L)_3) \quad (1)$$

where $E(Sc(L)_3)$ is the total energy of an Sc precursor with three ligands, $E(Sc(L)_2)$ is the total energy of an Sc precursor after loss of one ligand and $E(L)$ is the total energy of the eliminated ligand, all calculated in the gas phase with the DFT set up given above.

2.2. MOCVD growth

$Al_{1-x}Sc_xN$/GaN heterostructures were grown by MOCVD with two different Sc precursors: $(EtCp)_2Sc$(bdma) and $(EtCp)_2Sc$(dtbt). These precursors have a low vapor pressure (p_{vapor}), which was determined by TGA. A close coupled showerhead MOCVD reactor equipped with a proprietary heated gas injection system customized for precursors with low p_{vapor},[19,24] and patented by Fraunhofer IAF,[21] was employed for the epitaxial growth. Trimethylaluminum (TMAl), trimethylgallium (TMGa), silane (SiH_4) and ammonia (NH_3) were the Al, Ga, Si and N sources, respectively. The carrier gas was hydrogen. Two types of $Al_{1-x}Sc_xN$-

based heterostructures were deposited on 4 inch *c*-plane Al_2O_3 substrates: up to 500 nm-thick AlScN layers were grown on 500 nm-thick AlN buffer layers for compositional analysis. The TMAl flow was 18 μmol min^{-1} and the $(EtCp)_2Sc(bdma)$ flow 27 μmol min^{-1}. The growth duration was 90 min. Further, 10 to 13 nm-thick AlScN barrier layers were grown on semi-insulating GaN buffers,[30] in order to examine the generated 2DEGs. The NH_3 flow was kept at 50 μmol min^{-1} for all $Al_{1-x}Sc_xN$/GaN heterostructures. A nominal AlN interlayer was inserted before the *ca.* 10 nm-thick AlScN barriers in order to enhance interface abruptness, increase n_s and reduce R_{sh}. Details on the effect of nominal AlN interlayers on $Al_{1-x}Sc_xN$/GaN heterostructures structural and electrical properties can be found in our previous works.[22,23] The structures were capped with a 10 nm-thick SiN_x *in situ* passivation. Two series of $Al_{1-x}Sc_xN$/GaN heterostructures are examined: first, the growth temperature of AlScN barriers was varied from 900 to 1200 °C for both precursors to investigate the effect of impurity incorporation. The best performing of these $Al_{1-x}Sc_xN$/GaN heterostructures were grown also on 4 inch 4H-SiC substrates. For AlScN growth with $(EtCp)_2Sc(bdma)$, the TMAl flow was kept at 9 μmol min^{-1} and the $(EtCp)_2Sc(bdma)$ flow at 13 μmol min^{-1}. The growth duration was 7 min 30 s. For the growth with $(EtCp)_2Sc(dtbt)$, the TMAl flow was kept at 18 μmol min^{-1} and the $(EtCp)_2Sc(dtbt)$ molar flow at 10 μmol min^{-1}. The growth duration was 3 min 45 s. Second, a series of $Al_{1-x}Sc_xN$/GaN heterostructures with Sc concentrations from 0.8 to 20.0% was grown with $(EtCp)_2Sc(dtbt)$ in order to investigate the structural and electrical characteristics of the $Al_{1-x}Sc_xN$/GaN heterostructures with varying Sc incorporation. The Sc concentration of 13 nm-thick barrier layers was varied by sweeping the $(EtCp)_2Sc(dtbt)$ molar flow linearly from 7 to 28 μmol min^{-1}. Sc concentrations from 0.8 to 20% were achieved.

2.3. Characterization

Depth profiles of the chemical composition of the layers were obtained with secondary ion mass spectrometry (SIMS) with a quadrupole system (Q-SIMS) and ToF-SIMS. The Sc concentration was determined by MCs^+ method by comparing the $AlCs^+/ScCs^+$ signal ratio to that of magnetron-sputtered AlScN reference samples that were previously calibrated by energy elastic recoil detection analysis.[31] Currently, there are no SIMS standards for oxygen and carbon in $Al_{1-x}Sc_xN$, due to the lack of pure reference samples with concentrations below the detection limit. Consequently, these concentrations cannot be determined. We conclude on the relative presence of impurities by analyzing the 2DEG characteristics of $Al_{1-x}Sc_xN$/GaN heterostructures and by comparing the C^-/Sc^- and $^{18}O^-/Sc^-$ ToF-SIMS signal intensity ratios in the negative ion mode measurements of layers with the same Sc concentration. The $Al_{1-x}Sc_xN$ barrier and SiN_x cap thicknesses were determined by combining HRXRD $\Theta/2\Theta$-scans around the 0002, 0004 and 0006 reflections of GaN and X-ray reflectometry (XRR). The morphology and surface roughness of the epilayers were examined by atomic force microscopy (AFM) in tapping mode. The electrical performance of the 2DEGs of the $Al_{1-x}Sc_xN$/GaN heterostructures was examined with contactless eddy-current sheet resistance (R_{sh}) and contactless Hall effect measurements at room temperature. The reported values are average values for R_{sh}, n_s and electron mobility (μ) determined from 17 evenly distributed points across the 4-inch wafers. Additionally, Hall effect measurements with alloyed Ti/Al-based contacts were performed to compare R_{sh}, n_s and μ at room temperature and at 77 K (under liquid nitrogen atmosphere). The presence of 2DEGs was additionally verified by capacitance voltage (*C–V*) measurements with a mercury probe. A detailed study of these *C–V* characteristics can be found elsewhere.[32] Theoretical values for the variation of n_s with the Sc concentration ($n_{s,sim}(x)$) were determined by 1D-Schrödinger Poisson simulations, with and without carbon impurity doping in the AlScN layers.

3. Results

3.1. Precursor decomposition

The precursor $(EtCp)_2Sc(bdma)$, shown in Fig. 1(a), has two ethylcyclopentadienyl (EtCp) ligands and one bis(dimethylamino) acetamidinato (bdma) ligand and thus twenty carbon atoms per Scandium atom. From the DFT calculation, these (EtCp) ligands have a ligand loss energy E_{diss} of 359.69 kJ mol^{-1}. For the other ligand, the (bdma) ligand, the ligand loss energy is E_{diss} of 338.69 kJ mol^{-1}. A lower E_{diss} indicates higher reactivity. Consequently, during the decomposition of the precursor, the (bdma) ligand is lost first, and then the (EtCp) ligands. The precursor $(EtCp)_2Sc(dtbt)$, shown in Fig. 1(b), contains twenty-two carbon atoms per Scandium atom. The two (EtCp) ligands have a computed E_{diss} of 378.07 kJ mol^{-1} and the di-*tert*-butyl-triazenido (dtbt) ligand has a E_{diss} of 396.45 kJ mol^{-1}. This molecule should lose the (EtCp) ligand first, followed by the (dtbt) ligand. Comparing the precursors, the E_{diss} of the ligands of $(EtCp)_2Sc(dtbt)$ are larger than those of $(EtCp)_2Sc(bdma)$, which suggests that $(EtCp)_2Sc(bdma)$ is more reactive than $(EtCp)_2Sc(dtbt)$. Consequently, it is expected that $(EtCp)_2Sc(bdma)$ allows for more efficient Scandium incorporation at lower growth temperatures than $(EtCp)_2Sc(dtbt)$. The E_{diss} of the Cp ligand of Cp_3Sc and Me ligand of TMAl were calculated for comparison using the same DFT setup as described in 2.1. The Cp ligand and the Me ligand had a E_{diss} of 275.95 kJ mol^{-1} and 338.66 kJ mol^{-1}, respectively. This shows that the Cp ligand is lost more easily than the (EtCp), (bdma) and (dtbt) ligands. Compared to Cp_3Sc, $(EtCp)_2Sc(bdma)$ and $(EtCp)_2Sc(dtbt)$ require more energy to lose ligands. In contrast, the E_{diss} for TMAl

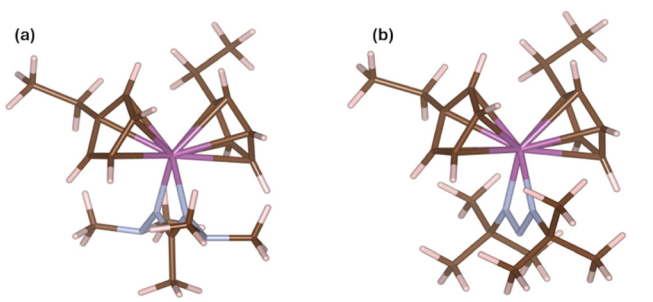

Fig. 1 Chemical structure of the Sc precursors calculated by DFT simulations. (a) $(EtCp)_2Sc(bdma)$ and (b) $(EtCp)_2Sc(dtbt)$. Sc is the purple rods, N is the light blue rods, C is the brown rods and H is the white rods.

is comparable with the (bdma) ligand of $(EtCp)_2Sc(bdma)$ and is more reactive that the (EtCp) ligands and (dtbt) ligand of $(EtCp)_2Sc(dtbt)$.

One (EtCp) ligand contains seven carbon atoms, that sums up to 14 carbon atoms in total for each $(EtCp)_2Sc(bdma)$ and $(EtCp)_2Sc(dtbt)$. The (bdma) ligand contains six carbon atoms, while the (dtbt) ligand contains eight carbon atoms. Under the assumption that the final ligands that are lost are more likely to incorporate into the film, $(EtCp)_2Sc(bdma)$ would be more likely to incorporate impurities from the (EtCp) ligands with their 14 carbon atoms, while $(EtCp)_2Sc(dtbt)$ would be more likely to incorporate the (dtbt) ligand that contains eight carbon atoms. It remains to explore whether the (EtCp) ligand itself has a different E_{diss} than the (bdma) and (dtbt) ligands, respectively, and how this affects carbon incorporation. In conclusion, lower carbon incorporation may be expected for $Al_{1-x}Sc_xN$ layers grown with $(EtCp)_2Sc(bdma)$ at lower temperatures compared to layers grown with $(EtCp)_2Sc(dtbt)$, considering the dissociation of the ligands from the Sc atom. If we take into account the sequence of the dissociation of the ligands and assume that ligand lost later incorporates preferentially, the precursor $(EtCp)_2Sc(bdma)$ with the (EtCp) ligands lost last might be more susceptible to carbon incorporation than $(EtCp)_2Sc(dtbt)$ with the (dtbt) ligand. Experimental investigation is necessary to shed light on this topic.

$(EtCp)_2Sc(bdma)$ has a slightly lower vapor pressure than $(EtCp)_2Sc(dtbt)$, as shown in Fig. 2(a). Compared to the first commercially available Sc precursor Cp_3Sc, p_{vapor} of both novel Sc precursors is increased by more than one order of magnitude. However, it is still far below that of bis-cyclopentadienyliron (Cp_2Fe), commonly used for Fe doping, and that of TMAl and TMGa, the conventional sources for Al and Ga. The E_{diss} of ligands is clearly independent of p_{vapor}. Both novel Sc precursors show good volatilization and a clean one step evaporation in the TGA shown in Fig. 2(b). The onset of 1% mass loss occurs at 90.94 °C for $(EtCp)_2Sc(bdma)$ and at 128.90 °C for $(EtCp)_2Sc(dtbt)$. Interestingly, $(EtCp)_2Sc(bdma)$ has a significant residual mass of 10%, while the one of $(EtCp)_2Sc(dtbt)$ is far below 1%. The cracking efficiency $\eta = 1 - e^{kt}$ *versus* temperature for residence times (t) of 10 ms and 100 ms is shown in Fig. 2(c). It is calculated using the Arrhenius equation for the rate constant $k = Ae^{-E_a/RT}$. A is the Arrhenius constant approximated as $\approx 10^{16}$ s^{-1}. The E_{diss} of the ligand that is lost first is used as the activation energy E_a in kJ mol^{-1}. R is the universal gas constant and T the absolute temperature in Kelvin. $(EtCp)_2Sc(bdma)$ clearly cracks more efficiently at lower temperatures than $(EtCp)_2Sc(dtbt)$. Longer residence times favor cracking.

Sc has a very low standard redox potential of −2.08 V and is therefore susceptible to oxidation.[33] In fact, the energies calculated for the interaction of $(EtCp)_2Sc(dtbt)$ with O_2 and H_2O are exothermic. The interaction with water is exothermic with a computed interaction energy of −0.38 eV, while the interaction energy with O_2 is −0.27 eV. Any presence of water or oxygen in the growth environment will consequently result in impurity contamination.

The most important characteristics of the two investigated Sc precursors are summarized in Table 1. For the epitaxial growth, both precursors were kept at 100 °C, achieving vapor pressures of 0.053 mbar for $(EtCp)_2Sc(bdma)$ and 0.176 mbar for $(EtCp)_2Sc(dtbt)$, respectively.

3.2. Incorporation of impurities in AlScN

Impurity incorporation in MOCVD-grown GaN and AlGaN is favored at low growth temperatures, low reactor pressures and low NH_3 flows.[12,34–37] The same trends were observed for AlScN grown with Cp_3Sc as Sc precursor.[38] Here, for AlScN grown with $(EtCp)_2Sc(bdma)$, incorporation of impurities was investigated on 500 nm-thick $Al_{0.75}Sc_{0.25}N$ layers grown on AlN/sapphire templates. The films were grown at low temperature of 900 °C at two different reactor pressures and NH_3 flows. Further a layer grown at 1200 °C is analyzed. The O_{18}^-/Sc^- and C^-/Sc^- ToF-SIMS signal intensity ratios strongly reflect the growth conditions and are further accompagnied by an unprecedented, distinct change in the coloration of the wafer, as illustrated in Fig. 3. The AlScN layer grown at 900 °C, 40 mbar and 180 mmol min^{-1} NH_3, shows a dark grey color and both high

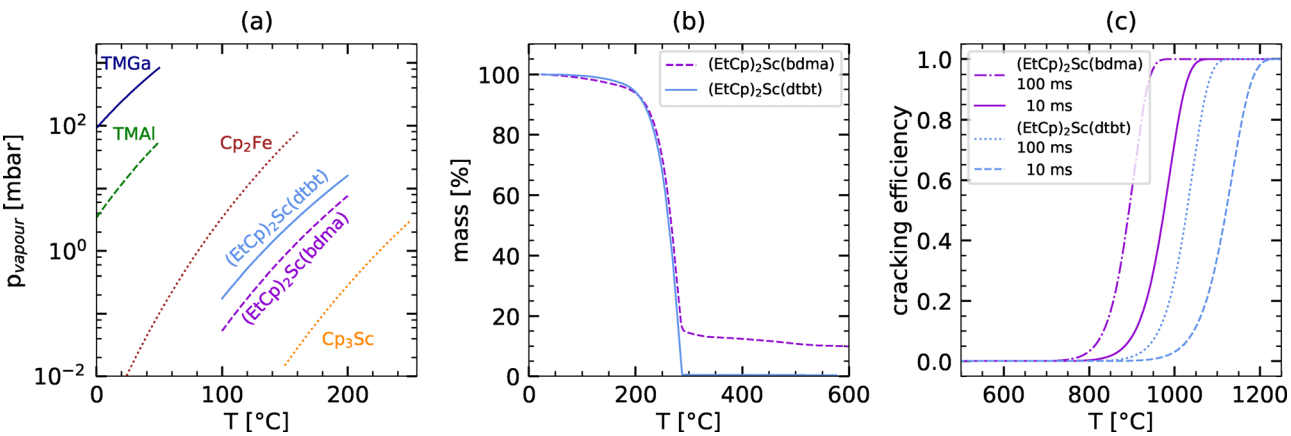

Fig. 2 The (a) vapor pressure in dependence of temperature for $(EtCp)_2Sc(bdma)$ and $(EtCp)_2Sc(dtbt)$, (b) the TGA analysis and (c) the calculated cracking efficiency in dependence of the growth temperature for different residence times. In (a), the vapor pressures of the conventional precursors TMGa, TMAl and Cp_2Fe and the first commercially available Scandium precursor Cp_3Sc are shown for reference.

Table 1 Characteristics of the Sc precursors $(EtCp)_2Sc(bdma)$ and $(EtCp)_2Sc(dtbt)$. T_{MP} is the melting point of the low melting solids in °C and the C/Sc ratio is the number of carbon atoms per Sc atom in the precursor molecule. The bond dissociation energies E_{diss} of the different ligands of the precursors were calculated by DFT simulations

	$(EtCp)_2Sc(bdma)$	$(EtCp)_2Sc(dtbt)$
Formula	$C_{20}H_{33}N_4Sc$	$C_{22}H_{36}N_3Sc$
T_{MP} [°C]	35	30
C/Sc	20	22
E_{diss} EtCp-ligand [kJ mol^{-1}]	359.69	378.07
E_{diss} bdma/dtbt-ligand [kJ mol^{-1}]	338.69	396.45

O_{18}^-/Sc^- and C^-/Sc^- ratios. The C^-/Sc^- ratio drops by one order of magnitude when the growth pressure is increased from 40 to 130 mbar at 900 °C and the coloration changes to a light grey. When the NH_3 flow gets reduced from 180 mmol min^{-1} to 25 mmol min^{-1} at 900 °C and 40 mbar, the C^-/Sc^- ratio increases by one order of magnitude and the coloration changes to an intense black. Since the O_{18}^-/Sc^- ratio remains largely unaffected by the change of growth conditions at 900 °C, the change in coloration can be attributed exclusively to the presence of carbon in the layers. When the growth temperature is increased to 1200 °C, the O_{18}^-/Sc^- ratio drops by two orders of magnitude. The C^-/Sc^- ratio drops by one order of magnitude at the same time. The sample features a distinct yellow-orange color. This color is associated with rocksalt ScN.[39] Indeed, the HRXRD phase analysis shows the peak associated with the rocksalt/zinc blende ScN 111 reflection (not shown). Similar distinct change in coloring with growth temperature was previously reported for AlYN, which was greyish at 900 °C, transparent at 1000 °C and showed the characteristic red of rocksalt YN at 1200 °C.[24]

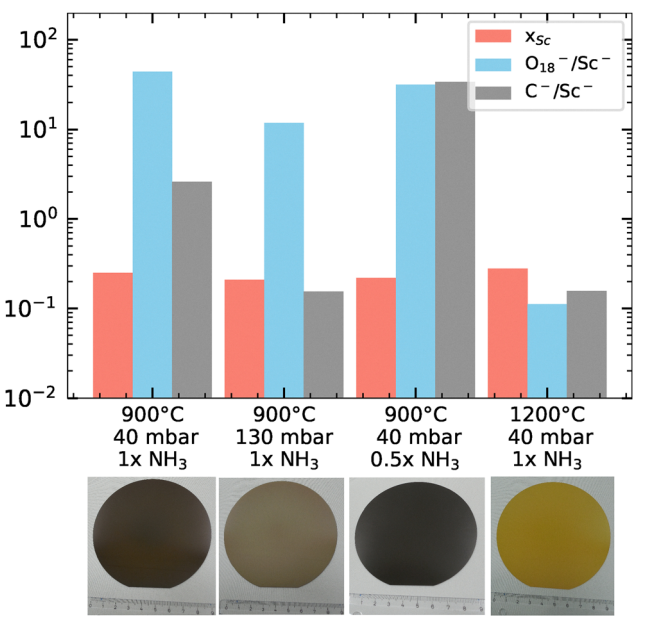

Fig. 3 O_{18}^-/Sc^- and C^-/Sc^- signal intensity ratios derived from ToF-SIMS measurements for 500 nm-thick $Al_{1-x}Sc_xN$ layers grown with a Sc concentration of approximately 25% at indicated conditions. The wafers show distinct coloring.

Variations in carbon incorporation can be attributed to a change in gas phase chemistry with temperature. High temperature supports the decomposition of the precursor molecules into gas phase radical species which subsequently react with radical hydrogen to byproducts that get removed from the growth surface. At lower temperature this process is less dynamic and fragments of the ligands get incorporated into the growing layer, leading to high carbon levels. This process is likely promoted by the high residual mass of the precursor $(EtCp)_2Sc(bdma)$ revealed with the TGA measurement shown in Fig. 2(b). The prominent presence of oxygen can be attributed to the above mentioned negative standard redox potential of −2.08 V of Sc.[33] Any background oxygen is readily incorporated. With rising temperature, metal-oxides get increasingly unstable due to the decreasing partial pressure of oxygen,[40] resulting in lower oxygen incorporation at higher growth temperatures, *e.g.* 1200 °C.

The exact concentrations of oxygen and carbon in the AlScN layers remain unknown, due to the lack of appropriate standards for oxygen and carbon quantification by ToF-SIMS.

It is important to note that, in a previous work, we presented a 250 nm-thick layer grown with $(EtCp)_2Sc(bdma)$ at 1000 °C that also exhibited high oxygen and carbon levels, but was transparent and ferroelectric.[41] It seems that specifically at 900 °C, the growth dynamics strongly favor carbon incorporation.

3.3. Electrical properties of AlScN/GaN heterostructures

The performance of the 2DEG formed at the barrier/channel interface is very sensitive to the incorporation of impurities and thus to different growth conditions that favor or suppress incorporation of impurities, especially to growth temperature. For 2DEGs in AlGaN/GaN heterostructures it was observed that increased carbon incorporation at low growth temperatures reduces n_s and increases R_{sh} to the point of complete degradation of the 2DEG.[12,42]

The same general observation is made for AlScN/GaN heterostructures grown with $(EtCp)_2Sc(bdma)$ and $(EtCp)_2Sc(dtbt)$. The R_{sh} of heterostructures grown at 900 °C is in the kΩ sq^{-1}-range (2590 and 1920 Ω sq^{-1}, respectively), as illustrated in Fig. 4(a). When the growth temperature of the AlScN barrier is increased to 1000 °C, the R_{sh} drops to 333 Ω sq^{-1} for $(EtCp)_2Sc(bdma)$ and 441 Ω sq^{-1} for $(EtCp)_2Sc(dtbt)$. At a growth temperature of 1100 °C, the lowest R_{sh} of 303 and 226 Ω sq^{-1} were achieved, with $(EtCp)_2Sc(bdma)$ and $(EtCp)_2Sc(dtbt)$, respectively. This temperature seems to be the optimum growth temperature in terms of 2DEG properties for both precursors. None of the approximately 10 nm-thick AlScN barrier layers grown at temperatures from 900 to 1200 °C show distinct coloring. The variation in R_{sh} with the temperature is not related to Sc composition variation, as the Sc concentration determined by Q-SIMS is independent of temperature in the range of 900 to 1100 °C, as illustrated in the inset of Fig. 4(a). Since the heterostructures grown with $(EtCp)_2Sc(bdma)$ have Sc concentrations of roughly 10% while those grown with $(EtCp)_2Sc(dtbt)$ have a Sc concentrations around 6%, a slightly higher R_{sh} is expected for $(EtCp)_2Sc(bdma)$ -grown heterostructures over $(EtCp)_2Sc(dtbt)$ grown samples. It is therefore interesting that

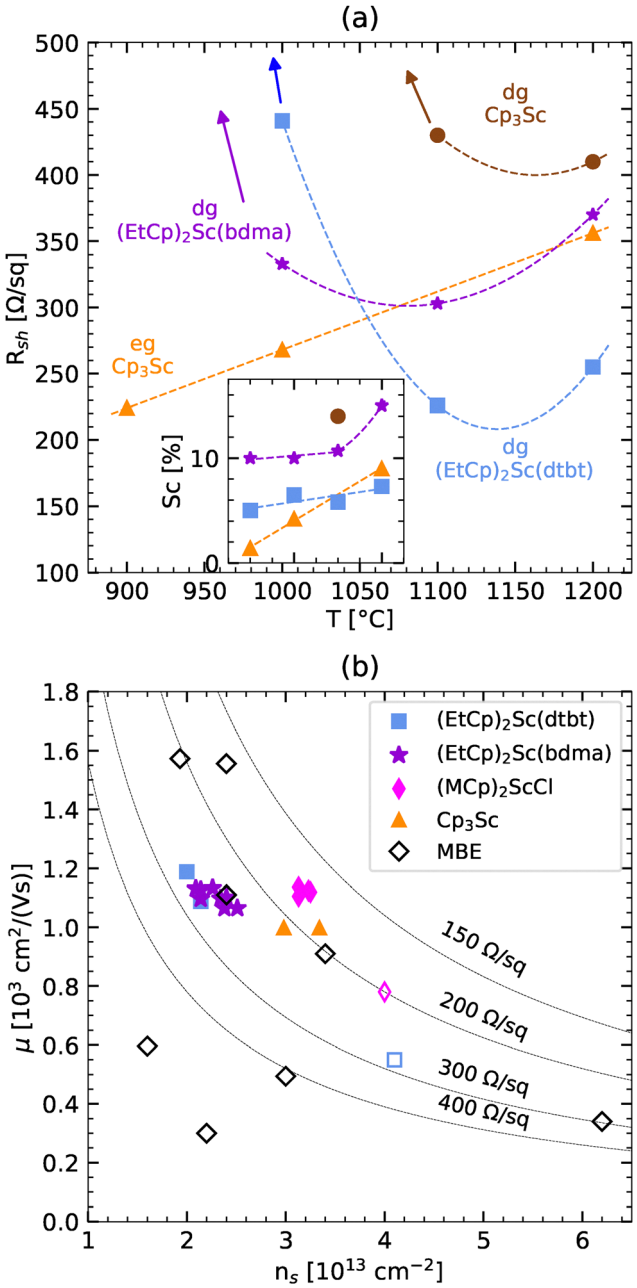

Fig. 4 (a) R_{sh} obtained with contactless eddy current measurements *versus* barrier growth temperature for $Al_{1-x}Sc_xN$/GaN heterostructures grown on Al_2O_3 substrates with development grade (dg) $(EtCp)_2Sc(bdma)$ and $(EtCp)_2Sc(dtbt)$. The values obtained with dg Cp_3Sc[43] and electronic grade (eg) Cp_3Sc[22] are shown for reference. The dashed lines are guides to the eye. The inset shows the Sc concentrations of determined by Q-SIMS. (b) The μ and n_s determined by contactless Hall effect measurements of $Al_{1-x}Sc_xN$/GaN heterostructures grown on 4H-SiC with the lowest R_{sh} achieved with the precursors $(EtCp)_2Sc(bdma)$ and $(EtCp)_2Sc(dtbt)$ in this work and Cp_3Sc and $(MCp)_2ScCl$ in our previous works.[20,22,44] The hollow markers indicate values reported by other groups, either by MOCVD,[45,46] or MBE.[47–52]

at 1000 °C, the R_{sh} of the heterostructure grown with $(EtCp)_2Sc(bdma)$ is lower than that of the one grown with $(EtCp)_2Sc(dtbt)$. A possible explanation for this lower R_{sh} is the difference in the energies for ligand loss. These are lower for $(EtCp)_2Sc(bdma)$ than for $(EtCp)_2Sc(dtbt)$, which might cause lower carbon incorporation and less carrier compensation at lower temperatures for $(EtCp)_2Sc(bdma)$ than for $(EtCp)_2Sc(dtbt)$. The lower R_{sh} achieved with $(EtCp)_2Sc(dtbt)$ than with $(EtCp)_2Sc(bdma)$ at 1100 and 1200 °C in turn can be attributed to the lower Sc concentrations, that lead to higher n_s and therefore lower R_{sh}. The increase in R_{sh} for the heterostructure grown with $(EtCp)_2Sc(bdma)$ at a growth temperature of 1200 °C can be attributed to increased Sc concentration as well as to increased interface degradation by the diffusion of atoms across the active interface.

The results from our previous studies with the Sc precursor Cp_3Sc further underline the effect of carbon incorporation on 2DEGs grown at different temperatures.[22,43] In this case a lower purity (development grade, dg) and a higher purity (electronic grade, eg) version of Cp_3Sc are compared. While the R_{sh} was in the kΩ sq^{-1}-range for layers grown at 900 and 1000 °C with dg Cp_3Sc, heterostructures grown with eg Cp_3Sc allowed for exceptionally low sheet resistances R_{sh} of approximately 224 Ω sq^{-1} at 900 °C, as shown in Fig. 4(a). This indicates that besides the carbon inherent to the precursor molecule, also the purity grade of the precursors affects the 2DEG performance strongly at lower barrier growth temperatures. The increase in R_{sh} with increasing temperature for heterostructure grown with eg Cp_3Sc clearly correlates with the Sc concentration that increases with the temperature as illustrated in the inset of Fig. 4(a). This shows that the low E_{diss} of the Cp ligands does not guarantee higher Sc incorporation at lower temperatures. Instead, the low p_{vapor} limits the arrival of Sc in the reactor and its incorporation into the film. This suggests that gas phase reactions promote Sc incorporation, or reduce Al incorporation, at higher temperatures.

Both $(EtCp)_2Sc(bdma)$ and $(EtCp)_2Sc(dtbt)$ employed in this study were qualified as development grade. Further purification might improve the electrical characteristics at low growth temperatures. Further, the addition of Ga to the AlScN barrier can reduce the incorporation of impurities significantly.[53] In fact, most recently, high electron mobility was achieved with $(EtCp)_2Sc(dtbt)$ as Sc precursor at temperatures between 900 and 1000 °C for quarternary AlGaScN barriers grown on GaN.[45] In such barriers the n_s is much lower than in ternary AlScN barriers and the existence of a lattice-matching to GaN remains to be explored.

A comparison of the electrical performance of $Al_{1-x}Sc_xN$/GaN heterostructures grown on 4H-SiC is shown in Fig. 4(b). Heterostructures grown with $(EtCp)_2Sc(bdma)$ and $(EtCp)_2Sc(dtbt)$ within this work, grown at 1100 °C, show high μ, higher than the highest values achieved previously with Cp_3Sc,[22] and similar to those reported with $(MCp)_2ScCl$, both obtained at 900 °C. However, the n_s is notably lower with the novel precursors. We assume that the increased growth rates prevent strong thermal budget-induced interface degradation at high growth temperature, even if the structural quality is not as high as at low temperatures.[23] Instead, we suspect that increased charge carrier compensation by carbon acceptors occurs when $(EtCp)_2Sc(bdma)$ or $(EtCp)_2Sc(dtbt)$ are employed.

3.4. AlScN/GaN grown with $(EtCp)_2Sc(dtbt)$

A series of AlScN/GaN heterostructures was grown at the optimum growth temperature of 1100 °C with the precursor $(EtCp)_2Sc(dtbt)$ to examine the variation of structural and electrical properties with varying Sc concentration. The Sc concentration of 13 nm-thick barrier layers was sweeped from 0.8 to 20% by adjusting the $(EtCp)_2Sc(dtbt)$ molar flow linearly from 7 to 28 μmol min^{-1}. The growth rate was 0.068 nm s^{-1}. A nominal AlN interlayer was inserted to further enhance interface abruptness.[23] In Fig. 5, the HRXRD $\Theta/2\Theta$-scans of the 0002, 0004 and 0006 reflection ranges are shown with the median Sc concentration determined by ToF-SIMS. The well defined AlScN peak and the high number of thickness fringes, that are present in all orders, indicate high structural quality of the barrier layers and abrupt interfaces to the underlying GaN. The AlScN peak shifts with increasing Sc concentration: towards higher $\Theta/2\Theta$ values at Sc concentrations up to 8.3% and towards lower $\Theta/2\Theta$ values at higher Sc concentrations. This behavior is attributed to the nonlinearity of the lattice parameters of AlScN with respect to the Al/Sc composition.

The Hall effect measurements results are shown in Fig. 6. The trend for n_s *versus* x_{Sc} depicted in Fig. 6(a) is in line with the trends expected from 1D Schrödinger-Poisson simulations (black dashed line). The decrease in n_s with increasing x_{Sc} correlates to a decrease in bandgap energy,[55] and spontaneous polarization with increasing x_{Sc}.[6] The latter reduces the built-in electric field across the barrier and thus the polarization induced sheet charge, which ultimately reduces the amount of charge carriers that accumulate in the potential well in the GaN channel, close to the heterointerface.[6] At the lattice-matched concentration, there is no piezoelectric contribution to the total polarization. Below (above) the lattice-matched concentration, the $Al_{1-x}Sc_xN$ layer is subject to biaxial tensile (compressive) strain, which leads to negative (positive) piezoelectric polarization and increases (decreases) the total n_s.[6] Interestingly, the n_s is by a factor of 1.7 lower than the values expected from theory. This can be caused by a combination of thermally degraded interfaces which enhance alloy scattering,[22,23] and the high carbon levels reported for MOCVD-grown AlScN layers. Acceptors trap electrons that would otherwise be available for the 2DEG and/or shield the electric field and reduce the n_s that way. The simulated $n_{s,sim}(x)$ can be matched to the experimental $n_{s,exp}(x)$ by adding a carbon doping to the AlScN layer that increases linearly from 2.47×10^{19} at a Sc concentration of 1% to 4.75×10^{19} at 25%. This is in the range of carbon concentration that was measured by SIMS in AlScN films grown with $(EtCp)_2Sc(dtbt)$ at similar conditions and published elsewhere.[44] Similar calculations were performed by Yassine *et al.*[32] to match n_s determined by *C–V* measurements on MIS structures fabricated on the same samples.

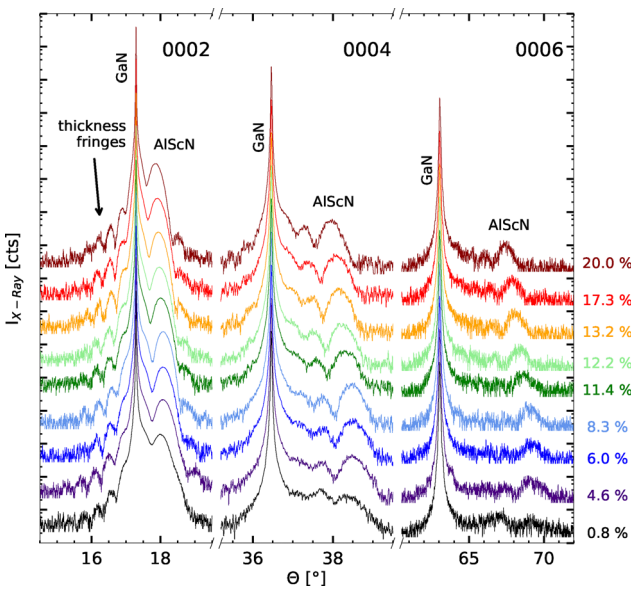

Fig. 5 HRXRD $\Theta/2\Theta$-scans of the 0002, 0004 and 0006 reflection ranges of $Al_{1-x}Sc_xN$/GaN heterostructures grown on Al_2O_3 substrates with Sc concentrations from 0.8 to 20%. The Sc concentration was determined by ToF-SIMS. The diffractogramms are shifted vertically for clarity.

With increasing Sc concentration and thus decreasing n_s, the R_{sh} increases, as shown in Fig. 6(b). The μ shows no particular trend. A decrease in electron–electron scattering with decreasing n_s could potentially increase the electron mobility and decrease the R_{sh} following the relation $R_{sh} = 1/e\mu n_s$. But here, the μ remains largely constant across the examined alloy concentration range and is not affected by the decrease in n_s at both room temperature and low temperature. Possibly, increased alloy scattering that is not shielded sufficiently by the growth of the nominal AlN interlayer counterbalances the decreasing electron–electron scattering. The fact that mobility doubles when the temperature is decreased from room temperature to 77 K while the n_s remains constant, proves unambiguously the presence of a 2DEG in most of the examined heterostructures. Only in the heterostructure with a Sc concentration of 0.8% no 2DEG was present and the R_{sh} in the kΩ-range. Excessive tensile strain had been released in the form of cracks, observed in DIC and AFM, as the critical thickness of $Al_{1-x}Sc_xN$ on GaN was exceeded. The heterostructure with a barrier with a Sc concentration of 4.6% featured with 242 Ω sq^{-1} the lowest R_{sh} and with 3.05×10^{13} cm^{-2} the highest n_s. As expected for a 2DEG, the n_s was found to be independent of temperature. The mobility increased from 546 to 953 $cm^2\ V^{-1}\ s^{-1}$ when the temperature was reduced from 298 to 77 K. However, this heterostructure showed significantly increased leakage current at negative voltages in *I–V* measurements performed with a mercury probe, other than the heterostructures with higher Sc content barriers. This can be attributed to modest relaxation effects.

3.5. Predictions for Y precursors

The growth of AlYN and AlYN/GaN heterostructures by MOCVD was reported with the yttrium precursors $(MCp)_3Y$,[5] and $(EtCp)_2$(iPr-amd)Y.[24] Other potential yttrium precursors with higher vapor pressures are the low-melting solids $(EtCp)_2Y(bdma)$ and $(EtCp)_2Y(dtbt)$, the structural twins to $(EtCp)_2Sc(bdma)$ and $(EtCp)_2Sc(dtbt)$, respectively, with an yttrium atom in place of a Sc atom. Analogue to $(EtCp)_2Sc(bdma)$, $(EtCp)_2Y(bdma)$ loses

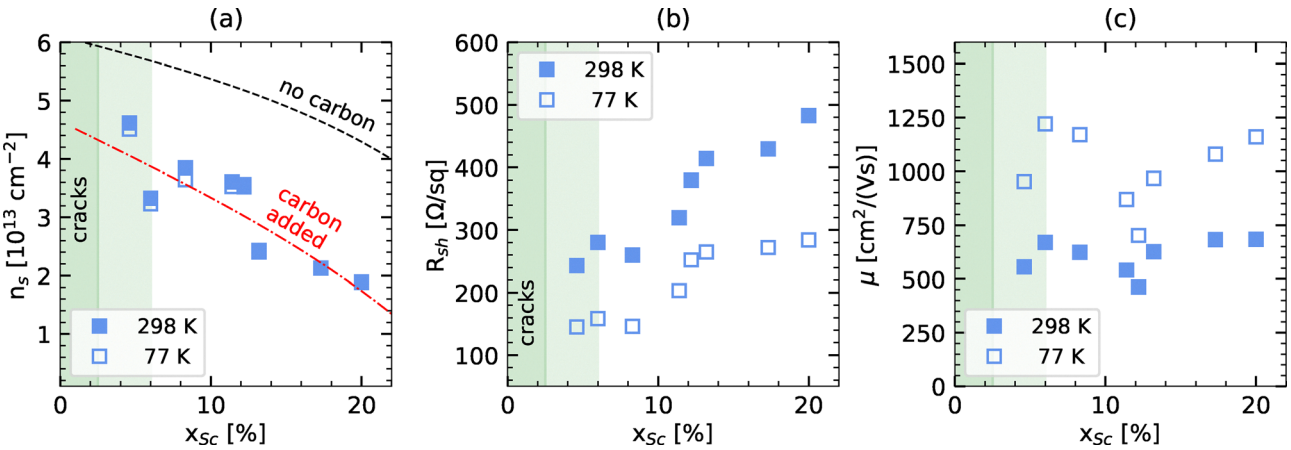

Fig. 6 (a) n_s, (b) R_{sh} and (c) μ determined by Hall effect measurements of 13 nm-thick $Al_{1-x}Sc_xN$/GaN heterostructures capped with SiN_x grown on Al_2O_3 substrates at room temperature (298 K) and under liquid N_2 atmosphere (77 K). The $n_s(x)$ calculated with the 1D Schrödinger-Poisson equation solver nextnano[54] without and with carbon doping is shown in (a). At low Sc concentrations, indicated in green, the layers were observed to crack (darkgreen) or show high leakage in I–V measurements of a mercury Schottky contact (lightgreen).

the (bdma) ligand first and the (EtCp) ligands second, with a computed E_{diss} of 399.07 kJ mol^{-1} and 465.09, respectively. $(EtCp)_2Y(dtbt)$, with two (EtCp) ligands and a (dtbt) ligand like $(EtCp)_2Sc(dtbt)$, loses the (EtCp) ligands first and the (dtbt) ligands second, with computed E_{diss} of 417.47 and 451.58 kJ mol^{-1}, respectively. The higher E_{diss} of the yttrium precursors compared to the scandium precursors is due to the higher bond enthalpies of yttrium–carbon and yttrium–nitrogen bonds compared to scandium–carbon and scandium–nitrogen bonds. These higher E_{diss} suggest that these yttrium precursors require higher process temperatures than the corresponding scandium precursors. It can be assumed that $(EtCp)_2Y(bdma)$ shows decomposition characteristics similar to $(EtCp)_2Sc(bdma)$ in terms of high residual mass, which makes $(EtCp)_2Y(dtbt)$ the more attractive option. The vapor pressure is similar to that of $(EtCp)_2Sc(dtbt)$, as illustrated in Fig. 7(a) and higher than those of the previously implemented yttrium precursors $(MCp)_3Y$ and $(EtCp)_2$ (iPr-amd)Y. The TGA in Fig. 7(b) shows that the onset if 1% mass loss occurs at 141.62 °C. The residual mass is below 1%. In Fig. 7(c) the cracking efficiency is shown, underlining that higher temperatures are required to achieve the same level of cracking as with the Sc counterpart $(EtCp)_2Sc(dtbt)$.

Y has a more negative standard redox potential than Sc and is therefore more susceptible to oxidation.[33] Similar to $(EtCp)_2Sc(dtbt)$, $(EtCp)_2Y(dtbt)$ reacts favorably with water, with a computed interaction energy of −0.74 eV, while the energy of interaction with O_2 is −0.10 eV, which is notably less exothermic. Thus, the presence of water during the process will potentially be more likely to lead to contamination compared to $(EtCp)_2Sc(dtbt)$. A summary of the most important characteristics of the two proposed Y precursors are listed in Table 2. Besides being a promising barrier material for HEMTs, AlYN is, like AlScN, piezo- and ferroelectric, and high quality growth by MOCVD will allow for applications in those fields, for example in non-volatile ferroelectric memories.[31,56,57]

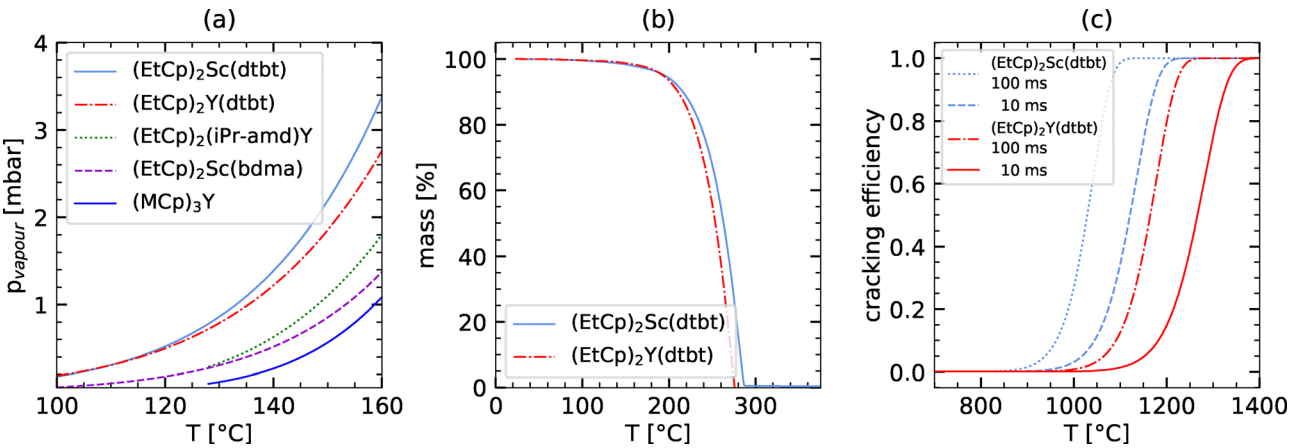

Fig. 7 The (a) vapor pressures in dependence of temperature for various yttrium precursors, including that of the scandium precursors $(EtCp)_2Sc(bdma)$ and $(EtCp)_2Sc(dtbt)$ for reference, and the (b) TGA data for $(EtCp)_2Y(dtbt)$, that is very similar to the one of its scandium twin $(EtCp)_2Sc(dtbt)$. (c) The cracking efficiencies of $(EtCp)_2Y(dtbt)$ and $(EtCp)_2Sc(dtbt)$ calculated using the Arrhenius equation are compared.

Table 2 Characteristics of the Y precursors $(EtCp)_2Y(bdma)$ and $(EtCp)_2Y(dtbt)$. T_{MP} is the melting point of the precursor in °C and the C/Y ratio is the number of carbon atoms per yttrium atom in the precursor molecule. The bond dissociation energies E_{diss} of the different ligands of the precursors were calculated by DFT simulations

	$(EtCp)_2Y(bdma)$	$(EtCp)_2Y(dtbt)$
Formula	$C_{20}H_{33}N_4Y$	$C_{22}H_{36}N_3Y$
T_{MP} [°C]	—	40
C/Y	20	22
E_{diss} EtCp-ligand [kJ mol^{-1}]	462.09	417.47
E_{diss} bdma/dtbt-ligand [kJ mol^{-1}]	399.07	451.58

4. Conclusions

This work shows how the decomposition behavior of the Scandium precursors $(EtCp)_2Sc(bdma)$ and $(EtCp)_2Sc(dtbt)$ relates to carbon incorporation and therefore the electrical characteristics of AlScN/GaN heterostructures. The lower bond dissociation energies E_{diss} of $(EtCp)_2Sc(bdma)$ provides higher reactivity at lower growth temperatures compared to $(EtCp)_2Sc(dtbt)$ but carbon-rich residues incorporate into the film, especially at a growth temperature of 900 °C. The negative impact of the impurity incorporation for both $(EtCp)_2Sc(bdma)$ and $(EtCp)_2Sc(dtbt)$ can be minimized by employing a growth temperature of 1100 °C and $Al_{1-x}Sc_xN$/GaN heterostructures with excellent structural quality and promising 2DEG characteristics are achieved. The growth of AlYN with $(EtCp)_2Y(dtbt)$ is predicted to be analogous to the growth of AlScN with $(EtCp)_2Sc(dtbt)$ but expected to require higher temperatures for precursor decomposition.

Conflicts of interest

There are no conflicts to declare.

Data availability

The data supporting this article have been included as part of the supplementary information (SI). Supplementary information: key interatomic distances from DFT relaxations. See DOI: https://doi.org/10.1039/d6ma00563b.

Acknowledgements

This work was funded by the BMBF Project ProMat_KMU "PuSH" Grant Number 03XP0387B. Dockweiler Chemicals GmbH supplied the Sc precursors for this study within the framework of this project. The authors thank Dr Christian Manz and Hanspeter Menner for their support during experiments.

References

1 R. Quay, P. Brückner, A. Tessmann, E. Ture, D. Schwantuschke, M. Dammann and P. Waltereit, *2017 Integrated Nonlinear Microwave and Millimetre-wave Circuits Workshop (INMMiC)*, **42017**, 1–3.
2 M. Meneghini, C. de Santi, I. Abid, M. Buffolo, M. Cioni, R. A. Khadar, L. Nela, N. Zagni, A. Chini, F. Medjdoub, G. Meneghesso, G. Verzellesi, E. Zanoni and E. Matioli, *J. Appl. Phys.*, 2021, **130**, 181101.
3 J. A. Del Alamo and E. S. Lee, *IEEE Trans. Electron Devices*, 2019, **66**, 4578–4590.
4 S. Zhang, W. Y. Fu, D. Holec, C. J. Humphreys and M. A. Moram, *J. Appl. Phys.*, 2013, **114**, 243516.
5 I. Streicher, P. Straňák, L. Kirste, M. Prescher, S. Müller and S. Leone, *APL Mater.*, 2024, **12**, 051109.
6 O. Ambacher, B. Christian, M. Yassine, M. Baeumler, S. Leone and R. Quay, *J. Appl. Phys.*, 2021, **129**, 204501.
7 T. Duarte, I. Streicher, P. Straňák, L. Kirste, M. Prescher, N. Wolff, S. Beuer, L. Kienle, R. Quay and S. Leone, *Adv. Mater. Interfaces*, 2025, e00726.
8 A. Asteris, T.-S. Nguyen, C. F. C. Chang, C. Savant, P. Lonergan, H. G. Xing and D. Jena, *J. Appl. Phys.*, 2026, **139**, 075708.
9 T.-S. Nguyen, N. Pieczulewski, C. Savant, J. J. P. Cooper, J. Casamento, R. S. Goldman, D. A. Muller, H. G. Xing and D. Jena, *APL Mater.*, 2024, **12**, 101117.
10 S. Krause, I. Streicher, P. Waltereit, L. Kirste, P. Bruckner and S. Leone, *IEEE Electron Device Lett.*, 2023, **44**, 17–20.
11 F. Ercolano, L. Balestra, S. Krause, S. Leone, I. Streicher, P. Waltereit, M. Dammann and S. Reggiani, *IEEE J. Electron Devices Soc.*, 2026, **14**, 1–9.
12 J.-T. Chen, U. Forsberg and E. Janzén, *Appl. Phys. Lett.*, 2013, **102**, 193506.
13 A. Y. Polyakov and I.-H. Lee, *Mater. Sci. Eng., R*, 2015, **94**, 1–56.
14 F. Brunner, E. Bahat-Treidel, M. Cho, C. Netzel, O. Hilt, J. Würfl and M. Weyers, *Phys. Status Solidi C*, 2011, **8**, 2427–2429.
15 Y.-H. Chen, T.-S. Nguyen, I. Streicher, J. Encomendero, S. Leone, H. G. Xing and D. Jena, *Appl. Phys. Lett.*, 2026, **128**, 042102.
16 S. Leone, T. Duarte, H. Menner, J. Richter, L. Kirste, S. Maegdefessel, F. Hoffmann, B. So and R. Quay, *Phys. Status Solidi A*, 2026, **223**, e202600005.
17 D. Koleske, J. Knapp, S. Lee, M. Crawford, J. Creighton, K. Cross and G. Thaler, *Issues associated with the metalorganic chemical vapor deposition of ScGaN and YGaN alloys*.
18 C. Saidi, N. Chaaben, A. Bchetnia, A. Fouzri, N. Sakly and B. El Jani, *Superlattices Microstruct.*, 2013, **60**, 120–128.
19 S. Leone, J. Ligl, C. Manz, L. Kirste, T. Fuchs, H. Menner, M. Prescher, J. Wiegert, A. Žukauskaitė, R. Quay and O. Ambacher, *Phys. Status Solidi RRL*, 2020, **14**, 1900535.
20 I. Streicher, S. Leone, L. Kirste, C. Manz, P. Straňá, M. Prescher, P. Waltereit, M. Mikulla, R. Quay and O. Ambacher, *Phys. Status Solidi RRL*, 2022, 2200387.
21 Fraunhofer Gesellschaft zur Förderung der Angewandten Forschung eV, Albert Ludwigs Universität Freiburg, US11996287B2 Method and apparatus for manufacturing a semiconductor layer and substrate provided therewith, 2024.
22 I. Streicher, S. Leone, C. Manz, L. Kirste, M. Prescher, P. Waltereit, M. Mikulla, R. Quay and O. Ambacher, *Cryst. Growth Des.*, 2023, **23**, 782–791.

23 I. Streicher, S. Leone, M. Zhang, T. S. Tlemcani, M. Bah, P. Straňák, L. Kirste, M. Prescher, A. Yassine, D. Alquier and O. Ambacher, *Adv. Funct. Mater.*, 2024, 2403027.

24 S. Leone, I. Streicher, M. Prescher, P. Straňák and L. Kirste, *Phys. Status Solidi RRL*, 2023, 2300091.

25 K. Nomoto, I. Streicher, T.-S. Nguyen, C. Savant, M. Ramesh, S. Ma, J. Encomendero, L. Kirste, P. Straňák, R. Quay, S. Leone, H. G. Xing and D. Jena, *Appl. Phys. Lett.*, 2025, **126**, 223509.

26 R. Ahlrichs, M. Bär, M. Häser, H. Horn and C. Kölmel, *Chem. Phys. Lett.*, 1989, **162**, 165–169.

27 Y. J. Franzke, C. Holzer, J. H. Andersen, T. Begušič, F. Bruder, S. Coriani, F. Della Sala, E. Fabiano, D. A. Fedotov, S. Fürst, S. Gillhuber, R. Grotjahn, M. Kaupp, M. Kehry, M. Krstic, F. Mack, S. Majumdar, B. D. Nguyen, S. M. Parker, F. Pauly, A. Pausch, E. Perlt, G. S. Phun, A. Rajabi, D. Rappoport, B. Samal, T. Schrader, M. Sharma, E. Tapavicza, R. S. TreB, V. Voora, A. Wodynski, J. M. Yu, B. Zerulla, F. Furche, C. Hättig, M. Sierka, D. P. Tew and F. Weigend, *J. Chem. Theory Comput.*, 2023, **19**, 6859–6890.

28 A. Schäfer, H. Horn and R. Ahlrichs, *J. Chem. Phys.*, 1992, **97**, 2571–2577.

29 F. Weigend and R. Ahlrichs, *Phys. Chem. Chem. Phys.*, 2005, **7**, 3297–3305.

30 S. Leone, F. Benkhelifa, L. Kirste, C. Manz, S. Mueller, R. Quay and T. Stadelmann, *Phys. Status Solidi B*, 2018, **255**, 1700377.

31 A. Zukauskaite, G. Wingqvist, J. Palisaitis, J. Jensen, P. O. Å. Persson, R. Matloub, P. Muralt, Y. Kim, J. Birch and L. Hultman, *J. Appl. Phys.*, 2012, **111**, 093527.

32 A. Yassine, M. Yassine, I. Streicher, R. Driad, L. Kirste, P. Straňák, P. Döring, S. Leone and O. Ambacher, *J. Appl. Phys.*, 2025, **137**, 194501.

33 P. Vanýsek, in *CRC handbook of chemistry and physics*, ed J. R. Rumble, CRC Press, Boca Raton and London and New York, 2022.

34 D. Koleske, A. Wickenden, R. Henry and M. Twigg, *J. Cryst. Grow.*, 2002, **242**, 55–69.

35 G. Parish, S. Keller, S. P. DenBaars and U. K. Mishra, *J. Electron. Mater.*, 2000, **29**, 15–20.

36 G. Koblmüller, R. M. Chu, A. Raman, U. K. Mishra and J. S. Speck, *J. Appl. Phys.*, 2010, **107**, 043527.

37 S. Leone, P. Brueckner, L. Kirste, P. Doering, T. Fuchs, S. Mueller, M. Prescher, R. Quay and O. Ambacher, *Phys. Status Solidi B*, 2020, **257**, 1900436.

38 J. Ligl, S. Leone, C. Manz, L. Kirste, P. Doering, T. Fuchs, M. Prescher and O. Ambacher, *J. Appl. Phys.*, 2020, **127**, 195704.

39 D. Gall, M. Städele, K. Järrendahl, I. Petrov, P. Desjardins, R. T. Haasch, T.-Y. Lee and J. E. Greene, *Phys. Rev. B: Condens. Matter Mater. Phys.*, 2001, **63**, 125119.

40 H. Ellingham, *J. Soc. Chem. Ind.*, 1944, **63**, 125–160.

41 N. Wolff, G. Schönweger, I. Streicher, M. R. Islam, N. Braun, P. Straňá, L. Kirste, M. Prescher, A. Lotnyk, H. Kohlstedt, S. Leone, L. Kienle and S. Fichtner, *Adv. Phys. Res.*, 2024, 2300113.

42 F. J. Lumbantoruan, Y.-Y. Wong, W.-C. Huang, H.-W. Yu and E.-Y. Chang, *J. Electron. Mater.*, 2017, **46**, 6104–6110.

43 J. Ligl, PhD thesis, University of Freiburg, 2020.

44 I. Streicher, Epitaxy of novel AlScN/GaN and AlYN/GaN heterostructures by metal-organic chemical vapour deposition, PhD thesis, 2024, DOI: 10.24406/publica-3744.

45 V. R. Muthuraj, C. E. Vozel, M. Kim, F. Wu, C. J. Clymore, A. Almogbel, S. Nakamura, J. S. Speck, U. K. Mishra, S. Keller and S. P. DenBaars, *Appl. Phys. Lett.*, 2026, **128**, 113308.

46 V. G. Thirupakuzi Vangipuram, A. Mukit, K. Zhang, S. Salmani-Rezaie and H. Zhao, *Cryst. Growth Des.*, 2026, **26**, 845–852.

47 J. Casamento, T.-S. Nguyen, Y. Cho, C. Savant, T. Vasen, S. Afroz, D. Hannan, H. Xing and D. Jena, *Appl. Phys. Lett.*, 2022, **121**, 192101.

48 K. Frei, PhD thesis, University of Freiburg, 2019.

49 A. J. Green, N. Moser, N. C. Miller, K. J. Liddy, M. Lindquist, M. Elliot, J. K. Gillespie, R. C. Fitch, R. Gilbert, D. E. Walker, E. Werner, A. Crespo, E. Beam, A. Xie, C. Lee, Y. Cao and K. D. Chabak, *IEEE Electron Device Lett.*, 2020, **41**, 1181–1184.

50 M. B. Tahhan, J. A. Logan, M. T. Hardy, M. G. Ancona, B. Schultz, B. Appleton, T. Kazior, D. J. Meyer and E. M. Chumbes, *IEEE Trans. Electron Devices*, 2022, **69**, 962–967.

51 S. El Whibi, N. Bhat, Y. Fouzi, N. De France, J.-C. De Jaeger, Z. Bougrioua, F. Bartoli, M. Hugues, Y. Cordier and M. Lesecq, *Appl. Phys. Express*, 2025, **18**, 046501.

52 K. Nomoto, J. Casamento, T.-S. Nguyen, L. Li, H. Lee, C. Savant, A. L. Hickman, T. Maeda, J. Encomendero, V. Gund, T. Vasen, S. Afroz, D. Hannan, J. C. M. Hwang, D. Jena and H. G. Xing, *Appl. Phys. Express*, 2025, **18**, 016506.

53 P. Wang, D. Wang, Y. Bi, B. Wang, J. Schwartz, R. Hovden and Z. Mi, *Appl. Phys. Lett.*, 2022, **120**, 012104.

54 S. Birner, *nextnano - Software for semiconductor nanodevices*, 29.07.2022, https://www.nextnano.de/.

55 M. Baeumler, Y. Lu, N. Kurz, L. Kirste, M. Prescher, T. Christoph, J. Wagner, A. Žukauskaitė and O. Ambacher, *J. Appl. Phys.*, 2019, **126**, 045715.

56 P. M. Mayrhofer, H. Riedl, H. Euchner, M. Stöger-Pollach, P. H. Mayrhofer, A. Bittner and U. Schmid, *Acta Mater.*, 2015, **100**, 81–89.

57 D. Wang, S. Mondal, J. Liu, M. Hu, P. Wang, S. Yang, D. Wang, Y. Xiao, Y. Wu, T. Ma and Z. Mi, *Appl. Phys. Lett.*, 2023, **123**, 033504.